Bubble velocity in horizontal and low−inclination upward slug flow in concentric and fully eccentric annuli

Roberto Ibarra[a],*, Jan Nossen[b]

Institute for Energy Technology (IFE), Kjeller, Norway, 2007

[a] *roberto.jose.ibarra-hernandez@ife.no*

[b] *jan.nossen@ife.no*

Corresponding author

Address: Department of Fluid Flow and Environmental Technology, Institute for Energy Technology, Instituttveien 18, Kjeller, Norway, 2007.

Telephone: +47 63 80 60 00

Keywords

Annulus flow; concentric; fully eccentric; slug flow; slug bubble velocity

Abstract

The Taylor bubble velocity for gas-liquid flows, which is of great importance in multiphase flow models, has been thoroughly studied for a wide range of conditions in full pipe flows. The applicability of models developed for these full pipe systems to flows in annuli has not been fully verified as very little data are available. This work presents experimental data on concentric and fully eccentric horizontal and 4° upward annulus for gas-liquid flows at high-pressure (400 kPa, absolute). The test fluids are water and Exxsol D60 as the liquid phases and sulphur hexafluoride (SF_6) as the gas phase. The test section consists of a 45 m long PVC pipe with an annulus pipe diameter ratio of $K = 0.505$ and an inside diameter of the outer pipe of 99 mm. Gamma densitometer sensors have been used to measure the instantaneous cross-sectional average holdup at different locations along the test section. Results show that the bubble velocity follows a linear trend, similar to that observed in full pipe systems, with a critical Froude number at $Fr_{M,C} \approx 3.3$. For Froude numbers lower than the critical value, the bubble velocity is well predicted by models developed for full pipe using the hydraulic diameter. For higher Froude numbers, a new correlation has been developed based on the experimental observations with excellent agreement for all cases studied.

1   Introduction

The co-current flow of gas and liquid in pipes can adopt a number of geometrical configurations or flow regimes depending on the velocity of the phases, the fluid properties, and the pipe system characteristics (*e.g.* pipe diameter and inclination). In general, these regimes are separated flows (stratified or annular), intermittent flows (*e.g.* slug), and dispersed flows (*e.g.* bubbly). Of these different configurations, slug flow is one of the most common flow regimes observed in industrial applications, such as oil and gas transportation pipelines, wells and risers. Slug flows are characterised by intermittent liquid regions, which fill the entire cross-section of the pipe, separated by gas pockets (Taylor bubbles) with a liquid film at the bottom region of the pipe (for horizontal and low-inclination pipes). The liquid slug flows faster than the liquid film ahead of it and is affected by a number of parameters, *e.g.* fluid properties, pipe diameter, pipe inclination, flow velocities, and more complex phenomena like gas entrainment in the liquid slug.

The Taylor bubble velocity, defined as the velocity of the three-dimensional bubble nose, has been thoroughly studied by a number of researchers for different flow conditions and fluid properties (*e.g.* liquid viscosities), see, for example, Davies and Taylor (1949), Collins *et al.* (1978), Bendiksen (1984), Hale (2000), Ujang (2003), and Bendiksen *et al.* (2018). In general, the gas bubble velocity can be modelled using the Nicklin *et al.* (1962) expression based on drift flux,

$$U_{\mathrm{B}} = C_{\mathrm{O}} U_{\mathrm{M}} + U_{\mathrm{d}}, \tag{1}$$

where C_{O} is the distribution parameter, U_{d} is the drift velocity of the bubble (in stagnant conditions), and U_{M} is the mixture velocity, which is defined as the total volumetric flow rate divided by the cross-sectional area of the pipe, $U_{\mathrm{M}} = Q_{\mathrm{T}}/A_{\mathrm{p}}$. The distribution parameter depends on the velocity profile of the liquid ahead of the gas bubble and can be estimated as the ratio of the maximum axial to the bulk velocity, *i.e.* $C_{\mathrm{O}} \approx 2$ for laminar flow and $C_{\mathrm{O}} \approx 1.2$ for turbulent flows. However, C_{O} also depends on other parameters, such as pipe diameter, pipe inclination,

and fluid properties; thus, the aforementioned approximation is only valid for a limited range of conditions. The drift velocity can be expressed as

$$U_d = Fr_d\sqrt{gD(1 - \rho_G/\rho_L)}, \tag{2}$$

where Fr_d is the dimensionless drift velocity, g is the gravitational acceleration, D is the pipe diameter, and ρ is the density of the gas and liquid phases, with subscripts G and L, respectively. The value of the coefficient Fr_d depends on the pipe inclination. For vertical flows, Dumitrescu (1943) found that $Fr_v = 0.351$ and for horizontal flows Benjamin (1968) obtained the value of $Fr_h = 0.542$. For inclined flows, extensions of the horizontal and vertical values have been performed by Bendiksen (1984) and Alves *et al.* (1993).

Bendiksen (1984) found that for turbulent low viscosity liquids in horizontal and low-inclination pipes, the tip of the bubble nose is located close to the top of the pipe (with $U_d > 0$) for Froude numbers lower than a critical value (gravity dominated conditions) which was found experimentally as $Fr_{M,C} \approx 3.5$. For higher Froude numbers, the bubble nose tip gradually moves towards the centre-line of the pipe with more liquid around the bubble at the top region of the pipe (with $U_d \approx 0$) increasing the value of the distribution parameter to that of the mean liquid axial velocity ratio as shown in Table 1.

**Table 1:** Bendiksen (1984) bubble velocity parameters.

Fr_M	C_O	Fr_d
< 3.5	$1.05 + 0.15\sin^2\theta$	$(Fr_v\sin\theta + Fr_h\cos\theta)$
≥ 3.5	1.2	0

where the mixture Froude number is defined as $Fr_M = U_M/\sqrt{gD(1 - \rho_G/\rho_L)}$.

Nuland (1998) proposed an expression for the distribution parameter in horizontal pipes as function of the inverse exponent in the power law velocity profile for turbulent flows, $C_{O,tur} = (n+1)(2n+1)/2n^2$, a constant value for laminar flows, $C_{O,lam} = 2$, and a linear interpolation between the turbulent and laminar C_O for the transitional region.

There exist in the literature a large number of correlations for the distribution parameter, C_O, and the drift velocity, U_d, (see Diaz and Nydal, 2016; and Lizarraga-Garcia *et al.*, 2017 for a review) for full pipe flows. However, very limited data are available for annulus pipe configurations. An annulus consists of two parallel pipes in which the fluids flow between the inside wall of the outer pipe and the outside wall of the inner pipe as shown in Figure 1. Annulus flows can be encountered in oil wells when gas, oil, water and/or drilling fluids flow between the production tubing and outer casing, between a gas injector and the production tubing, or between coiled tubing (inserted into the well from above) and the production tubing.

The annulus pipe configuration can be defined by the diameter ratio ($K = D_2/D_1$) and the relative position of the inner and outer pipe centres (*i.e.* degree of eccentricity, E), where D_1 is the inside diameter of the outer pipe and D_2 the outside diameter of the inner pipe. The degree of eccentricity is defined as $E = 2\delta/(D_1-D_2)$, where δ is the distance between pipe centres. The non-circular geometry of the annulus requires the definition of a hydraulic diameter. A number of researchers have attempted to develop hydraulic diameter expressions that represent the configuration of the annulus system, see, for example, Lam (1945), Knudsen and Katz (1958), Crittendon (1959), and Omurlu and Ozbayoglu (2007). However, in this study, we use the basic definition of the hydraulic diameter which is based on the flow area and the wetted perimeter, $D_h = D_1-D_2$.
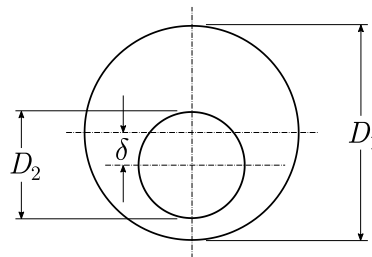
Figure 1: Annulus geometrical parameters.

A common assumption for the prediction of two-phase flow parameters in annulus pipe configurations is to adopt the models developed for full pipe geometry using the hydraulic diameter definition. This basic approach does not account for the complex phenomena

encountered in the new geometric configuration, *e.g.* changes in velocity distribution, phase distribution, and secondary flows, leading to significant prediction errors. Caetano *et al.* (1992a, b) presented an expression for the gas bubble velocity in upward vertical gas-liquid slug flows in concentric annulus based on the expression developed by Sadatomi *et al.* (1982) for the rise velocity which adopts an equi-periphery diameter as the characteristic dimension,

$$U_{\mathrm{B}} = 1.2 U_{\mathrm{M}} + 0.345 \sqrt{g(D_1 + D_2)}, \tag{3}$$

which in terms of the pipe diameter ratio yields

$$U_{\mathrm{B}} = 1.2 U_{\mathrm{M}} + 0.345 \sqrt{1 + K} \sqrt{g D_1}. \tag{4}$$

Hasan and Kabir (1992) found that the bubble nose becomes sharper in annulus configurations (with the presence of an inner pipe) and C_{O} varies slightly for different pipe diameter ratios thus suggesting a value of 1.2. They developed an expression for concentric annulus in vertical upward flows as

$$U_{\mathrm{B}} = 1.2 U_{\mathrm{M}} + (0.345 + 0.1K) \sqrt{g D_1 (1 - \rho_{\mathrm{G}}/\rho_{\mathrm{L}})}. \tag{5}$$

The above equation follows the suggestion by Griffith (1964) of using the inside diameter of the outer pipe, D_1, as the characteristic dimension for the rise velocity. Griffith (1964) also found that the gas bubble velocity increases with the pipe diameter ratio.

The above review shows that only limited work has been performed for the Taylor bubble velocity in concentric upward vertical two-phase flows, and only for low-pressure systems. There is a lack of data in the literature for horizontal and near-horizontal two-phase flows in concentric and eccentric annuli. This work aims to cover this gap presenting new Taylor bubble velocity data in large diameter concentric and fully eccentric annuli at high-pressure systems using a dense gas and liquid phases with two different viscosities to achieve a better representation of real field conditions.

2 Experimental Setup

2.1 *Flow facility, apparatus and test fluids*

The experimental investigations were performed in the Well Flow Loop located at IFE as shown in Figure 2 (see also Nossen *et al.*, 2017; for investigations of gas-liquid and liquid-liquid flow in a concentric annulus using the same flow facility). The experimental facility allows the investigation of three-phase flows using a range of advanced flow measurement techniques; however, this work has been limited to gas-liquid flows only. The test fluids used in this investigation were tap water and oil (Exxsol D60) as the liquid phases, and sulphur hexafluoride (SF_6) as the gas phase (Table 2 shows the physical properties of the test fluids). The SF_6 gas was selected due to the high density (being approximately 6 times higher than that of air) allowing a better representation of the conditions found in industrial applications, *e.g.* offshore gas-oil systems.
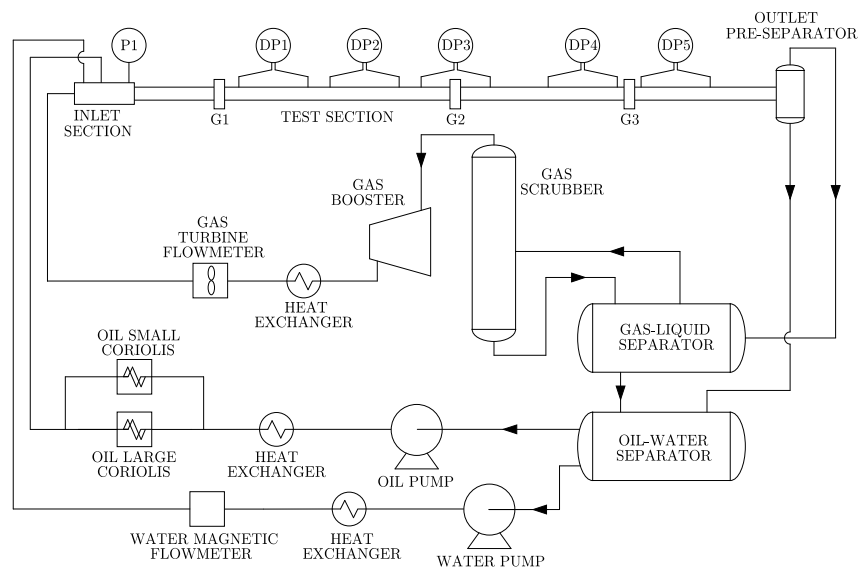
Figure 2: Schematic of the experimental flow loop (P1: absolute pressure sensor, DP1-5: differential pressure transducers, G1-3: gamma densitometers).

The flow loop consists of gas-liquid and liquid-liquid gravity-driven separators with a capacity of 0.8 m^3 and 4 m^3, respectively. The gas phase flows through a scrubber before entering the gas booster. The scrubber is used to remove any liquid remaining in the gas stream. The gas

booster consists of a three-stage compressor, driven by an electrical motor, with a capacity of 1000 Sm^3/h. The gas volumetric flow rate is measured, at inlet conditions, with a turbine flowmeter with an accuracy of ±1.5% of the actual flow. Two centrifugal pumps, with a capacity of 45 m^3/h each, are used for the water and oil phases. The water volumetric flow rate is measured with an electromagnetic flowmeter with a capacity of 0 – 60 m^3/h, and an accuracy of ±0.5% of the actual flow. The oil line was equipped with a set of two Coriolis mass flow meters with capacities of 40 – 20000 and 80 – 40000 kg/h (0.05 – 25 and 0.1 – 50 m^3/h based on the Exxsol D60 density) and accuracy of ±0.2% of the actual flow. The gas and liquid injection lines are equipped with heat exchangers to maintain a constant temperature throughout the experimental campaign.

Table 2: Physical properties of the test fluids at ~400 kPa (abs.) and ~20 °C.

	Density, ρ (kg/m^3)	Viscosity, μ (mPa.s) at Atm	Surface tension, σ (mN/m), to gas phase
SF$_6$ (gas)	23.9	0.015 ± 0.002	–
Exxsol D60	802	1.4 ± 0.02	28.8 ± 0.1
Tap water	998	1.04 ± 0.02	71.8 ± 0.2

The inlet section consists of three channels with splitter plates to promote stratification at the exit of the plates. The gas phase is injected in-line with the test section and flows through the upper channel. The oil and water phases are injected horizontally at 90° from the inlet section and flow through the centre and bottom channels, respectively. A flow straightener, installed downstream of the inlet section, is used to remove swirl generated by the inlet geometry configuration. The annulus test section, made of PVC, has a total length of 45 m with an inside diameter of the outer pipe, D_1, of 99 mm and an outside diameter of the inner pipe, D_2, of 50 mm. This results in a diameter ratio of $K = 0.505$ and a hydraulic diameter of $D_h = 49$ mm. Experiments cover concentric ($E = 0$) and fully eccentric ($E = 1$) annuli with the inner pipe located at the bottom of the outer pipe. The inner pipe extends over the entire length of the test section and was positioned using specially designed supports to minimise the effect on the flow.

2.2   Instrumentation

The test section is equipped with 5 differential pressure transducers installed along the pipe with an accuracy of ±0.1% of the span (set to 6 kPa). Pressure transducers are located at $L/D_h = 284$, 410, 501, 649, and 719, with L the distance from the inlet, and measure the pressure drop, ΔP, over an axial length of $62D_h$, $40D_h$, $50D_h$, $38D_h$, and $64D_h$, respectively. The pressure at the inlet section (P1 in Figure 2) is measured with an absolute pressure sensor with an accuracy of ±0.5% of the full scale (0 – 1 MPa, absolute). The instantaneous cross-sectional average holdup, H_L, has been measured with 3 broad-beam gamma densitometers at a sampling frequency of 50 Hz for a total recording time of 100 s. From experience, an optimum balance between temporal resolution and signal-to-noise ratio is achieved with the selected sampling frequency. The holdup measurement is based on the attenuation of the gamma rays between the source and the detector. These gamma densitometers are located at $L/D_h = 256$, 520, and 704. Calibration of the gamma densitometers was performed by measuring the transmitted intensity for single-phase gas, oil and water. The respective intensity calibration (*e.g.* gas and oil) was then used to calculate the holdup for two-phase flows.

Four Photron Mini UX100 high-speed cameras, with a maximum resolution of 1280×1024 pixels at a maximum frame-rate of 4 kHz, have been used to capture instantaneous images of the flow installed at $L/D_h = 124$, 540, 740, and 766 (cameras 1, 2, 3, and 4). The first three cameras are equipped with a 14-mm ultra-wide-angle lens and set to a frame-rate of 50 Hz to capture large-scale features. The fourth camera, equipped with a Nikkor 60-mm lens, is set to a frame-rate of 1 kHz to capture fast-, small-scale features.

2.3   Flow conditions and experimental procedure

A total of 478 slug flow conditions were covered using gas-oil and gas-water flows at pipe inclinations, θ, of 0° and 4° (concentric and fully eccentric) for various superficial velocities, defined for phase i as $U_{Si} = Q_i/A_P$ where Q is the volumetric flow rate and A_P the cross-sectional

area of the annulus, $A_P = \pi(D_1^2 - D_2^2)/4$. Superficial gas velocities at inlet conditions, $U_{SG,inlet}$, were varied between 0.5 and 5 m/s and superficial liquid velocities, U_{SL}, between 0.2 and 2 m/s with steps of 0.2 m/s. Experiments were performed at steady-state conditions at a pressure of 400 kPa (absolute) and temperature of 21 ± 1 °C. The pressure drop along the test section affects the density of the gas phase, *i.e.* the gas expands increasing its velocity (the effect on liquids can be neglected). This velocity increase can be significant at conditions of high gas velocities and high liquid rates resulting in large deviations as compared with values at inlet conditions. Thus, a correction must be introduced to account for the pressure difference between the inlet section and the location of interest using the expression $U_{SG} = U_{SG,in-situ} = U_{SG,inlet} (\rho_{G,inlet}/\rho_{G,in-situ})$. For example, the gas superficial velocity to be used in the analysis of the gas bubble velocity between gamma densitometers 2 and 3 is corrected using the calculated pressure at the mid-point between G2 and G3 from the test section pressure gradient and the absolute pressure at the inlet. Results below for the gas bubble velocity are presented in terms of in-situ U_{SG} using the aforementioned correction, which in turn modifies U_M and Fr_M.

Uncertainty analysis of the measured flow parameters has been performed based on the systematic errors and standard deviation of the samples (random standard uncertainty) which propagate to the calculated quantities (Dieck, 2006). Table 3 shows the average uncertainty estimates of the system parameters.

**Table 3:** Uncertainty estimates.

Variables	Uncertainty
D_1 (mm)	±0.55 mm
D_2 (mm)	±0.28 mm
θ (°)	±0.04°
ρ_G (kg/m^3)	±0.5 kg/m^3
ρ_L (kg/m^3)	±1.5 kg/m^3
U_{SG} (m/s)	±2.3 %
U_{SL} (m/s)	±1.7 %
H_L	±1.5%
$\Delta P/\Delta L$ (Pa/m)	±4.5%

3   Results and Discussion

The purpose of the present work is to investigate the velocity of gas bubbles in slug flow in horizontal and low-inclination upward concentric and eccentric annulus configurations. Results are presented in terms of mean bubble velocity based on the total recording time from the gamma densitometer measurements, as well as analysis of the bubble nose shape, and bubble velocity for single slugs including the effect of the corresponding slug length. This offers an insight into the behaviour of slug flow in annulus configurations to determine the applicability of models developed for full pipe systems. Reported bubble velocity data, U_B, corresponds to in-situ conditions between gamma sensors G2 and G3, unless explicitly stated otherwise.

3.1   *Mean slug bubble velocity*

The time-evolution of the cross-sectional average holdup is obtained from the gamma densitometers, which are synchronised to start recordings at the same time (no initial lag). These holdup profiles show the characteristics of slug flow, *i.e.* regions of high liquid holdup followed by gas pockets. The cross-correlation between two different holdup profiles, as shown in Figure 3, provides the overall time lag, t_lag. Then, the mean or global slug bubble velocity can be calculated from $U_\mathrm{B} = \Delta x / t_\mathrm{lag}$, where Δx is the distance between gamma sensors. The uncertainty of the bubble velocity for the different flow conditions studied, based on the acquisition frequency, is estimated to be between 0.4 and 1.9% depending on the flow velocity. This means that the selected acquisition frequency is sufficient to capture the gas bubble velocity with low uncertainty based on the distance between gamma sensors.
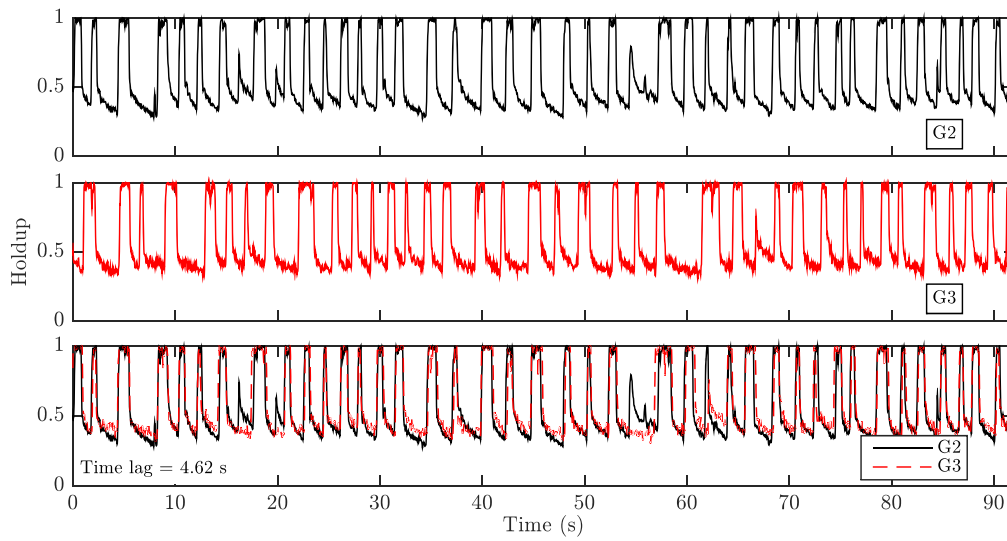
Figure 3: Example of the time-evolution of the cross-sectional average holdup from gamma sensors G2 (top) and G3 (middle) along with the shifted profile comparison (bottom) based on the cross-correlation time lag. Holdup profiles correspond to gas-oil flow in a horizontal concentric annulus ($U_{SL} = 0.6$ m/s, $U_{SG,inlet} = 0.75$ m/s).

Figure 4 shows the experimental slug bubble velocity as function of the in-situ mixture velocity for gas-water and gas-oil flows in concentric and fully eccentric annulus at 0° and 4° inclination. Bubble velocities follow approximately linear trends and are well predicted using the Nicklin *et al.* (1962) expression, see Eq. (1), with different experimental values of C_O and U_d depending on the fluids, annulus eccentricity, and pipe inclination. For each combination and increasing the mixture velocity, there is a change in the linear trend at a critical mixture Froude number, $Fr_{M,C}$, of about 3.3, which yields a mixture velocity of approximately 2.2 m/s. In Figure 4, $U_{B,L}$ corresponds to the trend at $Fr_{M,C} < 3.3$ and $U_{B,H}$ corresponds to the trend at $Fr_{M,C} \geq 3.3$. Note that the Froude numbers for annuli are calculated using the hydraulic diameter, D_h. The approximate value of $Fr_{M,C}$ is consistent for all different fluids, annulus eccentricities, and inclinations studied. Bendiksen (1984) found this critical transition at $Fr_{M,C} \approx 3.5$ for full pipe systems of diameters 19.2 and 24.2 mm.

Experimental C_O and U_d values were obtained from linear fitting of the slug bubble velocity as function of the mixture velocity. There is very low deviation between the linear trend

(equations are shown in Figure 4) and the experimental slug bubble velocity. Statistical parameters are shown in Table 4. This indicates that the development of the slug bubble velocity with the mixture velocity is quite uniform and stable and can be predicted with a linear relationship. A definition of the error statistical parameters is presented in Appendix A.
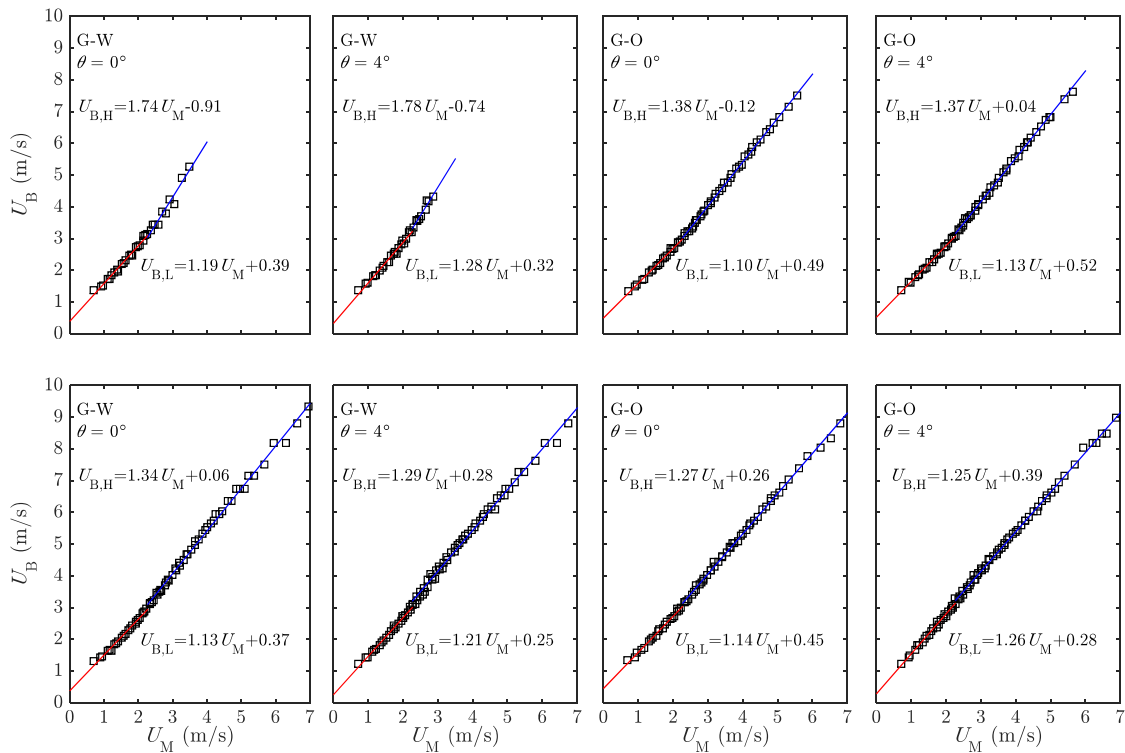

Figure 4: Experimental slug bubble velocity as function of in-situ mixture velocities, U_M, for concentric annulus (top) and fully eccentric annulus (bottom).

Table 4: Error statistical parameters of the slug bubble linear trend and experiments.

			e_1 (%)		e_2 (%)		e_3 (%)	
			$Fr_M < 3.3$	$Fr_M \geq 3.3$	$Fr_M < 3.3$	$Fr_M \geq 3.3$	$Fr_M < 3.3$	$Fr_M \geq 3.3$
CON	G-W	0°	-0.04	0.09	2.00	3.22	3.24	3.88
		4°	-0.06	0.04	2.27	1.54	3.15	1.98
	G-O	0°	-0.03	0.03	1.47	0.78	2.11	1.01
		4°	-0.02	0.05	1.47	0.99	1.89	1.23
ECC	G-W	0°	-0.05	0.13	1.76	1.52	2.84	1.82
		4°	-0.06	0.17	1.92	2.03	2.69	2.53
	G-O	0°	-0.01	0.07	1.51	0.95	2.35	1.27
		4°	-0.01	0.05	1.78	0.94	2.24	1.38

Note that limited data are shown in concentric gas-water flows as compared with the other cases. Concentric gas-water slug flow showed an unstable behaviour with no uniform slugs at high Froude numbers. The transition to churn or transitional flows occurs at lower superficial gas velocities, for a given superficial liquid velocity, than those observed in all other flow cases. This might be attributed to wettability effects, *i.e.* the oil tends to wet the pipe creating a continuous thin film at the pipe wall in the gas region for high gas velocities, whereas for gas-water flows, this film is not continuous. The wettability of the outer wall of the inner pipe affects the shape of the front of the liquid slugs. For concentric gas-water flows at high *Fr*, there is no continuous liquid film around the wall of the inner pipe. This creates filaments or liquid ejection from the slug front that further creates instabilities in the flow (see Figure 5a). On the other hand, in concentric gas-oil flows, the front of the liquid slug has a more uniform shape (see Figure 5b). The continuous oil layer at the pipe wall (inner pipe) prevents the front of the liquid slug from breaking into filaments or jets.


(a)

(b)
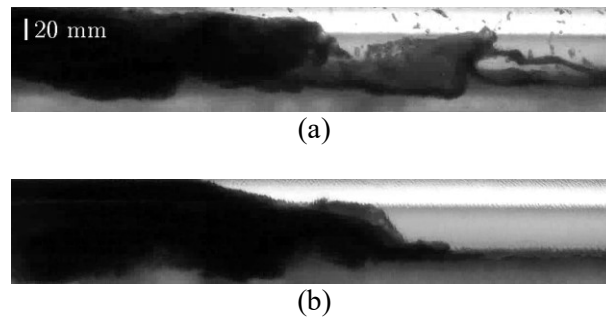
Figure 5: Instantaneous images of liquid slug front from camera-3 (located at $L/D_h = 740$) for gas-water (a) and gas-oil (b) for horizontal concentric annulus at $U_{SL} = 0.8$ m/s and $U_{SG,inlet} = 1.5$ m/s ($Fr_M \approx 3.5$).

The aforementioned behaviour was not observed in the fully eccentric gas-water annulus experiments as the inner pipe was located at the bottom region of the outer pipe, thus, for our experimental test matrix, the inner pipe was always covered by liquid.

The ratio between the slug bubble velocity and the mixture velocity as function of the Froude number is presented in Figure 6. This relation offers an insight into the behaviour of the distribution parameter, C_O, and the drift velocity, U_d. In general, the ratio U_B/U_M sharply

decreases with increasing Froude number (in the region where $U_d > 0$) to a fairly constant value at $Fr_M \geq Fr_{M,C}$ where the horizontal trend indicates that $U_d \to 0$ and $C_O \approx U_B/U_M$. However, there seems to be a transitional region at approximately $3 < Fr_M < 6$ where the ratio U_B/U_M increases with the Froude number. The trend is more prominent in gas-water flows. In these regions, where the slope of U_B/U_M is higher than 0, the "drift velocity" is lower than 0.
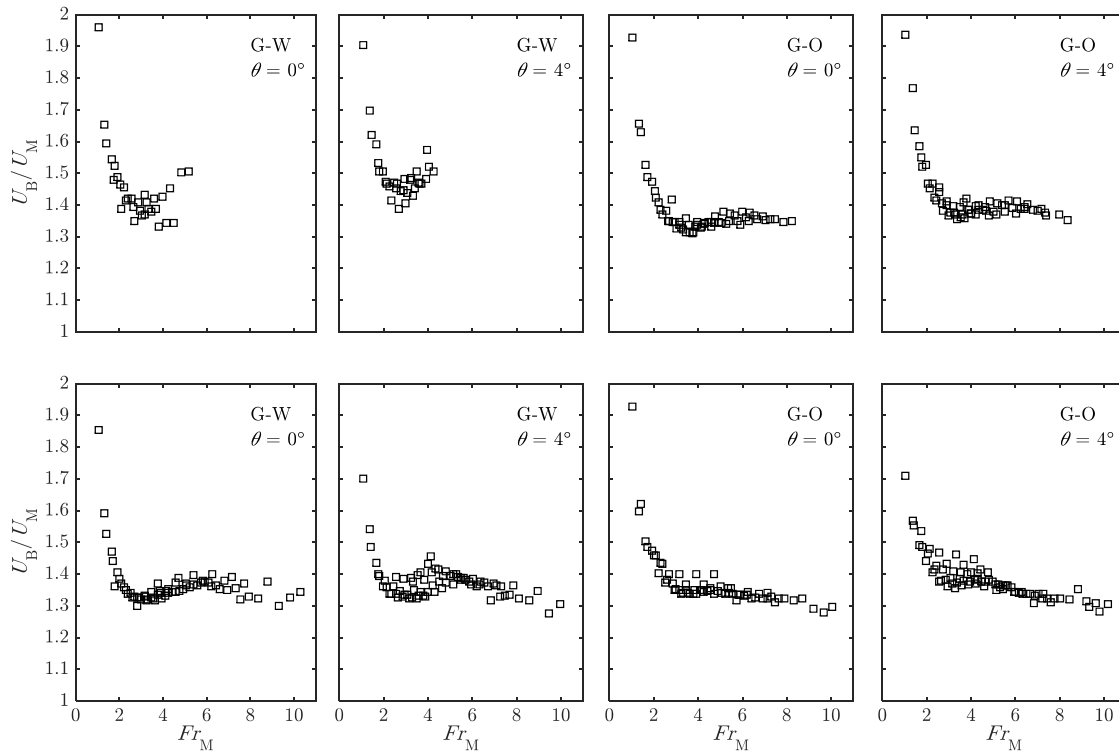
Figure 6: Slug bubble velocity to mixture velocity ratio as function of the mixture Froude number, Fr_M, for concentric annulus (top) and fully eccentric annulus (bottom).

The overall drift velocity for $Fr_M > Fr_{M,C}$ (see second right-hand term in equations in Figure 4) is close to or higher than zero. However, for concentric gas-water flows, the drift velocity obtained from the linear trend (for $Fr_M > Fr_{M,C}$) is -0.91 m/s and -0.74 m/s for inclinations of 0° and 4°, respectively. These negative U_d values represent only the transitional region where the ratio U_B/U_M increases with Fr_M. Limited data are available at high Froude numbers. This also affects the experimental distribution parameter values, for the same region, resulting in significantly larger values ($C_O > 1.4$) compared with other flow cases.

Figure 7 shows values of the distribution parameter, C_O, (from linear fitting) for each flow type as function of the pipe inclination. For Froude numbers lower than the critical value ($Fr_M < Fr_{M,C}$), the only clear trend is that C_O values increase with the pipe inclinations for a given annulus type and liquid viscosity, which was also observed by Bendiksen (1984). While it is true that there is no well-defined difference in trends between concentric and fully eccentric annulus flows, C_O values are closely bounded between 1.1 and 1.3 for all cases. For $Fr_M \geq Fr_{M,C}$, C_O seems to be fairly constant with the pipe inclination with C_O values bounded between 1.25 and 1.38, with the exception of concentric gas-water flows. Distribution parameter values are consistent with the type of flow of the liquid slug ahead of the gas bubble, *i.e.* C_O can be estimated as the ratio of the maximum axial velocity to the bulk or average velocity for turbulent flow, $Re_M > 4000$. Reynolds numbers for the present study are shown in Table 5, where $Re_M = \rho_L U_M D_h / \mu_L$. This assumption has been confirmed by Polonsky *et al.* (1999) who measured the velocity field ahead of the gas bubble in vertical flows using Particle Imaging Velocimetry (PIV). They found that the experimental distribution parameter, C_O, agrees with the ratio of the maximum to the average velocity from the profile obtained in the PIV field.
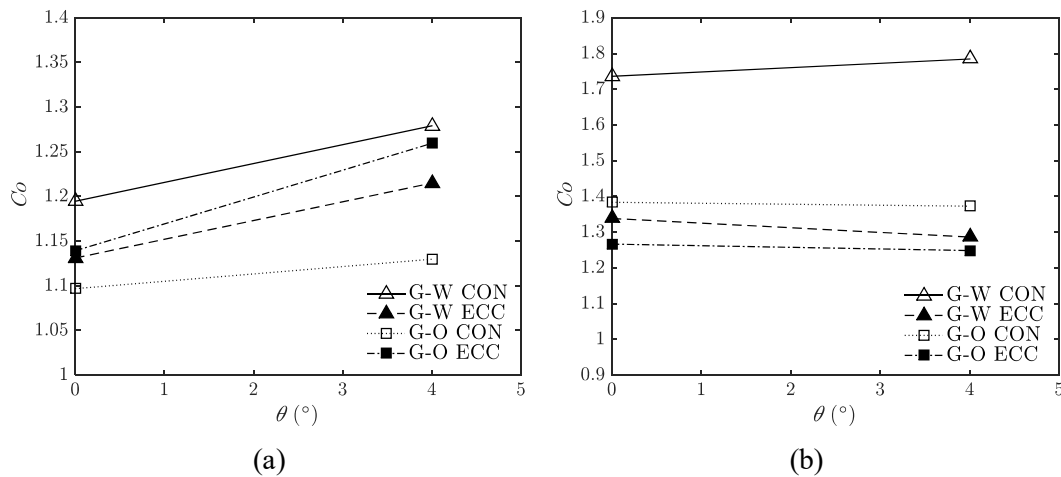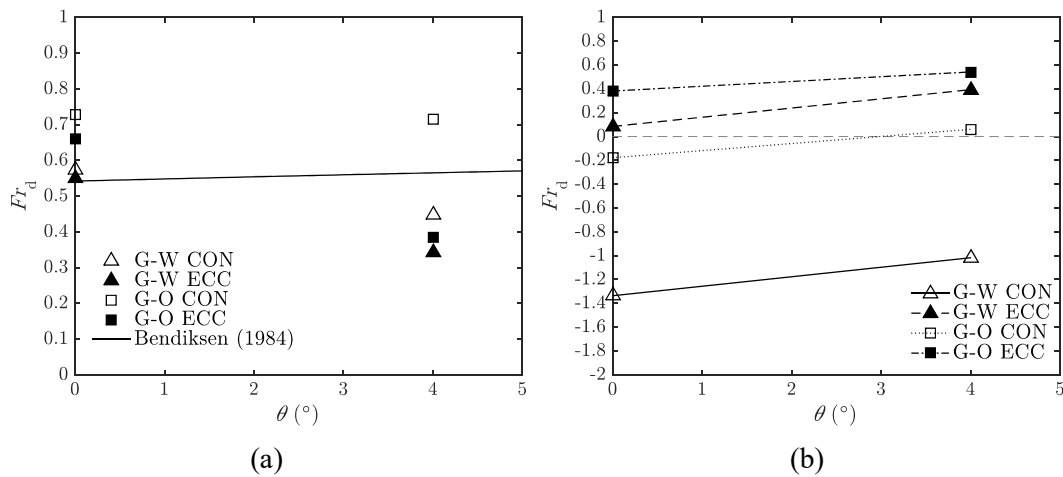

Figure 7: Distribution parameter, C_O, as function of the pipe inclination, θ, for gas-water and gas-oil in concentric and fully eccentric annulus for: (a) $Fr_M < Fr_{M,C}$, and (b) $Fr_M \geq Fr_{M,C}$.

Table 5: Reynolds number range for the present study.

Flow	Re_M
Gas-water	33 000 – 320 000
Gas-oil	19 000 – 196 000

Dimensionless drift velocity values, Fr_d, are shown in Figure 8 as function of the pipe inclination. For $Fr_M < Fr_{M,C}$ and $\theta = 0°$, Fr_d values are bounded between 0.55 to 0.57 and 0.66 to 0.73 for gas-water and gas-oil flows, respectively. The values for gas-water flows are close to that found by Benjamin (1968) ($Fr_h = 0.542$). For $Fr_M \geq Fr_{M,C}$, Fr_d values slightly increase with the pipe inclination, as contrary to that observed at low Fr_M, with values bounded between -0.2 to 0.5 (with the exception of gas-water flows in concentric annulus). This behaviour is not observed in full pipe flows in which $U_d \rightarrow 0$.


Figure 8: Dimensionless bubble drift velocity, Fr_d, as function of the pipe inclination, θ, for gas-water and gas-oil in concentric and fully eccentric annulus for: (a) $Fr_M < Fr_{M,C}$, and (b) $Fr_M \geq Fr_{M,C}$.

The development of the distribution parameter and drift velocity can be related to the shape of the bubble and the location of the tip of the nose. For horizontal and upward inclined full pipe systems, C_O increases and U_d decreases as the tip of the bubble nose move from the top of the pipe towards the centre-line.

3.2   Slug bubble shape

Instantaneous images from the camera recordings located at $L/D_h = 740$ (camera-3) have been analysed to detect the shape of the gas bubble. At low velocities, there is low gas entrainment in the liquid slug. This means that the shape of the bubble can be easily detected from the raw images with no further treatment. At higher velocities, the significant gas entrainment and the presence of a liquid film around the pipe walls obstruct the direct detection of the bubble edge, thus, image post-processing must be performed, *e.g.* convert to binary and perform morphological operations on the binary image.

Figure 9 shows shapes of the bubble nose for concentric and fully eccentric horizontal annulus flows for a Froude number lower than the critical value ($Fr_M \approx 2.0$). The tip of the bubble nose is located at the top of the outer pipe with the exception of concentric gas-water flows in which the tip is located around the centre-line of the pipe. This results in higher C_O values for the latter case matching the ratio of the maximum axial to the bulk velocity, *i.e.* $C_O = 1.2$ for turbulent flows. For other cases, *i.e.* concentric gas-oil and fully eccentric flows, C_O values are bounded between 1.10 and 1.13 following the relation between the location of the bubble nose tip and the local axial to bulk velocity ratio. The difference in the nose tip location for concentric gas-water flows with respect to other cases might be attributed to the wettability effects described above.

(a) Concentric gas-water   (b) Eccentric gas-water

(c) Concentric gas-oil   (d) Eccentric gas-oil
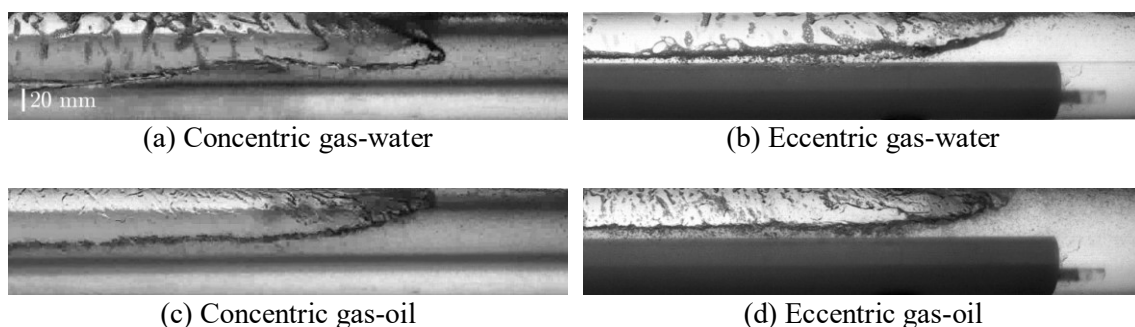
Figure 9: Shapes of the bubble nose for gas-water and gas-oil horizontal concentric and fully eccentric annulus flows at $U_{SL} = 0.6$ m/s and $U_{SG,inlet} = 0.75$ m/s ($Fr_M \approx 2.0$) from camera-3.

Figure 10 shows the bubble nose edge detection for gas-water and gas-oil horizontal concentric annulus for a Froude number higher than the critical value ($Fr_M \approx 3.4$). The location of the nose tip for gas-water flow is consistent with findings from lower Fr_M values (see Figure 9a) with the nose tip located at the centre-line of the pipe. For concentric gas-oil flows, the bubble nose has a pointed bullet shape with liquid encapsulation at the top of the outer pipe and the tip moves towards the centre-line of the pipe (see Figure 10d2) from that location for lower Fr_M values (see Figure 9b). Therefore, the distribution parameter increases and, in general, the drift decreases.

Note that the flow instantaneous images from Figure 9 and Figure 10 are distorted by the circular shape of the pipe and the difference in the refractive indices between the fluids and the pipe material (no correction box was used at the location of the camera).

(a1) (a2)

(b1) (b2)

(c1) (c2)

(d1) (d2)
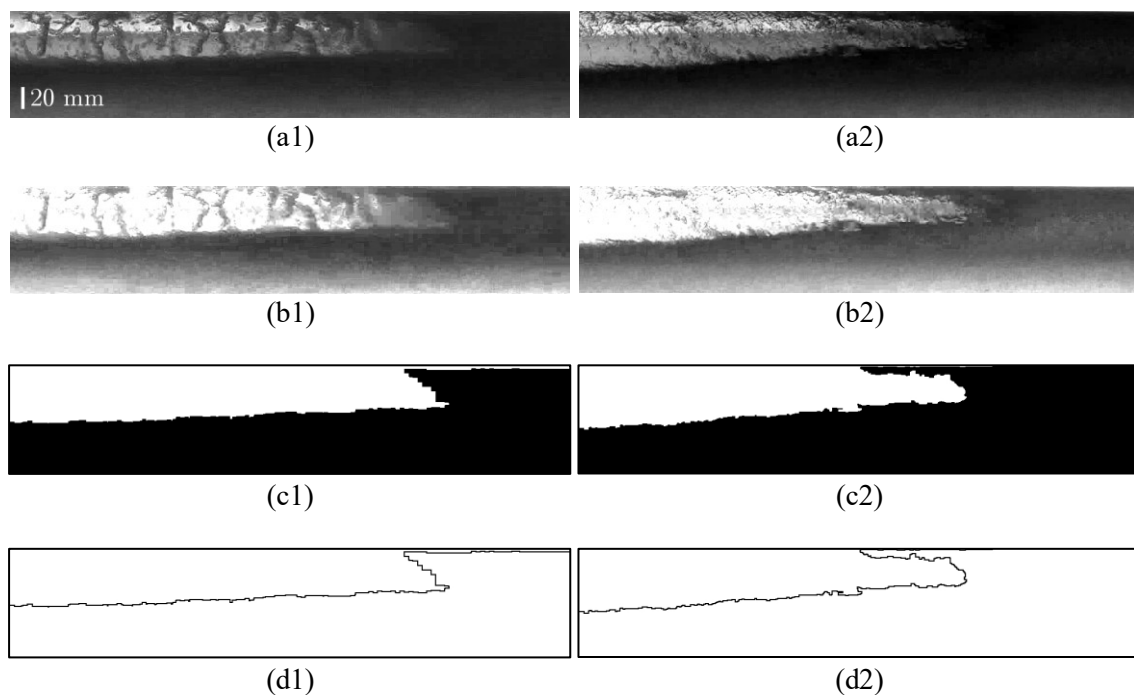
Figure 10: Image processing for bubble nose profile detection from camera-3 for gas-water (left column, denoted 1) and gas-oil (right column, denoted 2) for horizontal concentric annulus at $U_{SL} = 0.8$ m/s and $U_{SG,inlet} = 1.5$ m/s ($Fr_M \approx 3.5$): (a) raw image, (b) processed image, (c) binary image after morphological operations, and (d) edge detection (bubble profile).

3.3 Individual slug bubble velocity

The cross-correlation of two holdup time sequences, as described in Section 3.1, returns the overall time lag between both profiles. This time lag is used to shift the downstream holdup profile to detect individual slugs that match those in the upstream holdup profile (see Figure 3). Liquid slugs are identified using a holdup threshold to distinguish slugs from large wave structures in the gas region. This allows the calculation of individual slug bubble velocities, $U_{B,i}$, and their corresponding slug lengths, L_S.

Few researchers have studied the relation between individual slug bubble velocities and slug lengths. Moissis and Griffith (1962) found that, for vertical flows, the bubble velocity decreases with an increase in L_S/D until a critical L_S value is reached above which the bubble velocity remains fairly constant. Fagundes Netto *et al.* (2001) performed experiments in horizontal water flows to study the behaviour of two isolated air bubbles flowing in the test section. They found that liquid slugs with initial lengths longer than a critical value ($L_{CRIT} = 6.3D$) grow in size with distance from the inlet. Conversely, gas bubbles coalesce for initial $L_S < L_{CRIT}$. Woods *et al.* (2006) studied the generation of slugs in air-water horizontal flows in 76.3 and 95 mm inside diameter pipes. They found that U_B is independent of the slug length; however, measurements of U_B were performed for $L_S > 6.6D$. This means that the criterion of the critical slug length could not be verified.

From our experimental data set, two representative flow conditions are selected to show the relation between the bubble velocity and the slug length in concentric and fully eccentric annulus flows, as presented in Figure 11 and Figure 12 for $Fr_M \approx 2.0$ and $Fr_M \approx 4.0$, respectively. It is noted that the slug bubble velocity is independent of the slug length. The average standard deviation of the bubble velocity for flow conditions in Figure 11 and Figure 12 is 2.63% and 2.26%, respectively (low scattering).
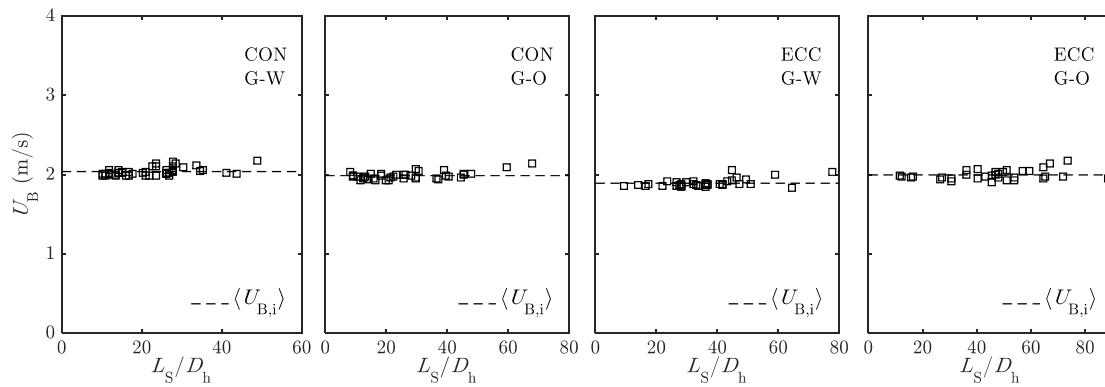
Figure 11: Individual slug bubble velocities as function of the corresponding slug length, L_S, normalised by the hydraulic diameter, D_h, for horizontal annuli at $U_{SL} = 0.6$ m/s and $U_{SG,inlet} = 0.75$ m/s ($Fr_M \approx 2.0$).

Bubble velocities with slug lengths lower than the critical value found by Fagundes Netto *et al.* (2001) follow the same linear trend as observed in Figure 11 and Figure 12. However, a detailed inspection of the holdup profiles from the gamma densitometers reveals that short liquid slugs, detected in the upstream gamma sensor, merged with the nearby slug before the location of the downstream gamma sensor. This means that the bubble velocity of these slugs cannot be determined from our experimental setup. Note that the occurrence of this merging is quite low.
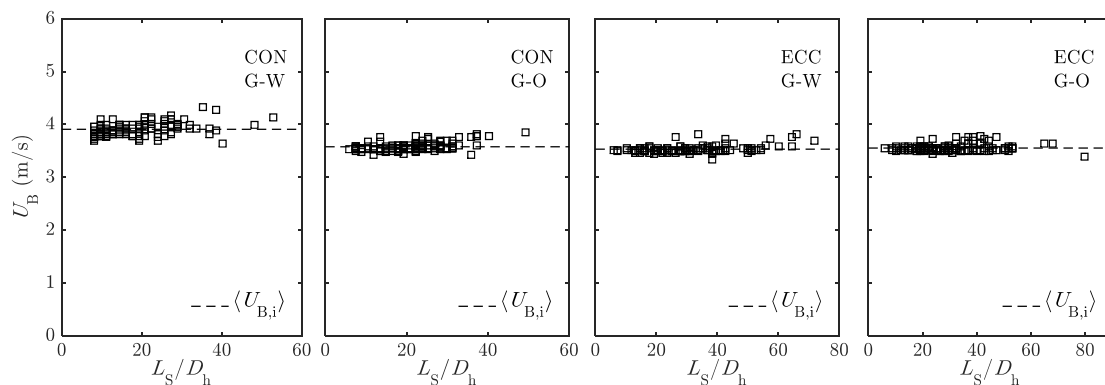

Figure 12: Individual slug bubble velocities as function of the corresponding slug length, L_S, normalised by the hydraulic diameter, D_h, for horizontal annuli at $U_{SL} = 1.6$ m/s and $U_{SG,inlet} = 1.0$ m/s ($Fr_M \approx 4.0$).

Figure 13 shows the slug merging for two different flow conditions. Here, short slugs flow at a faster velocity than the mean U_B (see dashed-squared region), thus merging with the slug ahead, which consequently grows in size. However, the length of these short slugs at the location

of the upstream gamma sensor is $L_S/D_h \approx 6.7$ and 7.5 for Figure 13a and b, respectively, which is larger than the critical length found by Fagundes Netto *et al.* (2001). Moreover, the minimum slug length for the given flow conditions in Figure 13a and b, for slugs that follow the linear trend (with values close to the mean), is $L_S/D_h = 5.7$ and 6.0, respectively.

Although it is not possible based on the present data alone to report the velocity of fast moving short slugs (as these merged before the location of the downstream gamma sensor), two different trends can be identified, as shown in Figure 14, for the slug bubble velocity as function of the slug length. These trends are (1) a constant U_B for entire range of L_S and (2) decreasing U_B with increasing L_S until a critical value.

(a)   (b)
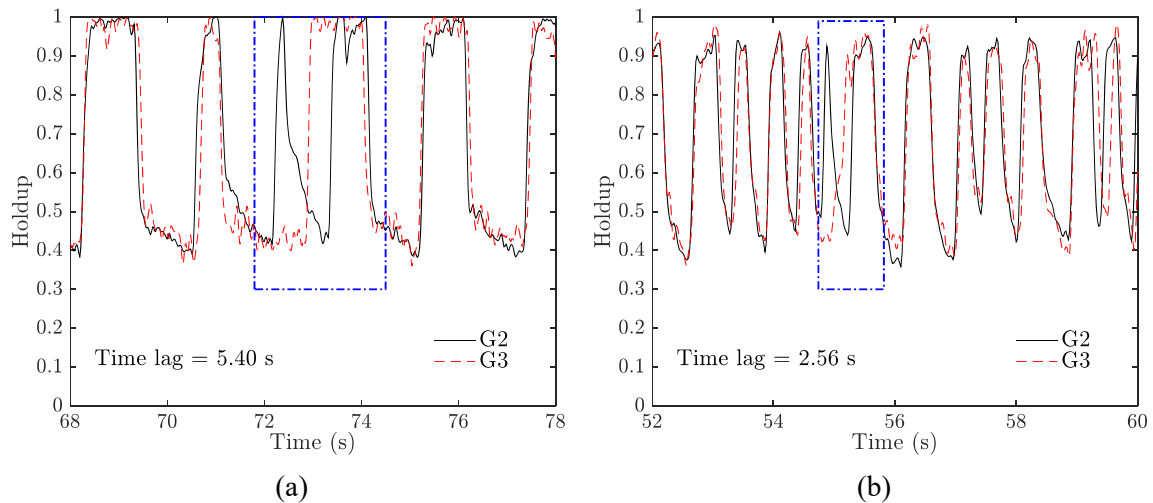
Figure 13: Time-evolution of the cross-sectional average holdup from gamma sensors G2 and the lagged profile from G3 for horizontal gas-oil concentric annulus showing the merging of two liquid slugs in the dash-squared region at: (a) $U_{SL} = 0.6$ m/s, $U_{SG,inlet} = 0.5$ m/s; and (b) $U_{SL} = 1.6$ m/s, $U_{SG,inlet} = 1.0$ m/s.
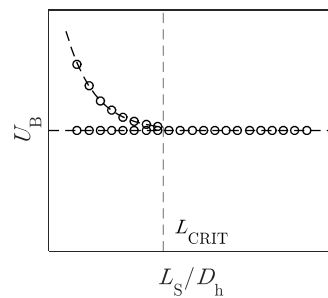
Figure 14: Representation of the two trends deduced from individual slug bubble velocity and slug length data.

3.4   Development of the slug bubble velocity

The development of the slug bubble velocity along the test section is presented in Figure 15 for the entire data set in terms of the U_B/U_M ratio between gamma sensor G1/G2 and G2/G3. Note that the corresponding mixture velocity is calculated based on the mid-position between gamma sensors to account for the expansion of the gas. This analysis shows that the global gas bubble velocity (from cross-correlation for each flow condition) normalised by the corresponding in-situ mixture velocity remains fairly constant along the test section with an absolute average error of less than 1.8% and 1.6%, for the concentric and fully eccentric annulus data, respectively.
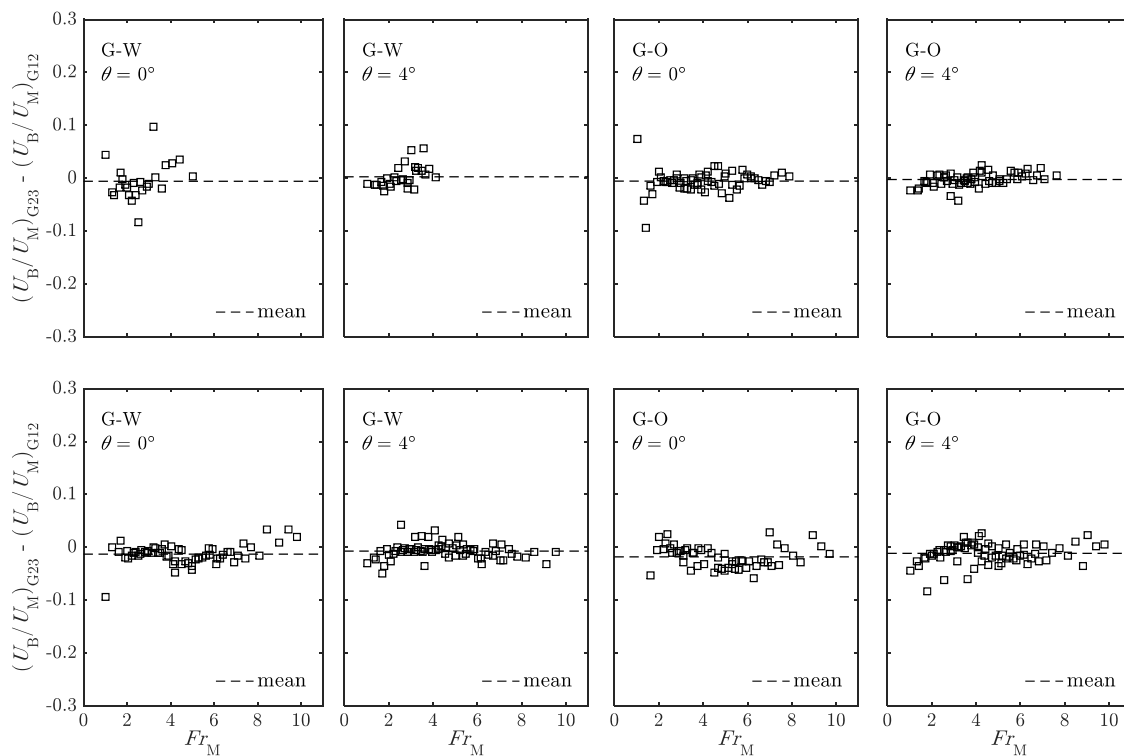
Figure 15: Slug bubble velocity difference from the cross-correlation between gamma sensors G1/G2 and G2/G3 as function of the mixture Froude number, Fr_M, for concentric annulus (top) and fully eccentric annulus (bottom).

3.5   Data comparison with models

Predictions from the Bendiksen (1984) and Smith *et al.* (2015) models have been compared with the experimental data. Bendiksen (1984) model follows the Nicklin *et al.* (1962) expression (Eq.

(1)) with parameters from Table 1, using the annulus hydraulic diameter for the calculation of the drift velocity. Smith *et al.* (2015) estimated the gas bubble velocity as the maximum value at low and high Froude numbers,

$$U_{\mathrm{B}} = \max\big(U_{\mathrm{B,low}}, U_{\mathrm{B,high}}\big), \tag{6}$$

where U_{B} low and high are based on the Nicklin *et al.* (1962) expression (Eq. (1)),

$$U_{\mathrm{B,low/high}} = C_{\mathrm{O,low/high}} U_{\mathrm{M}} + U_{\mathrm{d,low/high}}. \tag{7}$$

The drift velocity, U_{d}, is

$$U_{\mathrm{d,low}} = (Fr_{\mathrm{v}} \sin\theta + Fr_{\mathrm{h}} \cos\theta)\sqrt{gD_{\mathrm{h}}(1 - \rho_{\mathrm{G}}/\rho_{\mathrm{L}})}, \tag{8}$$

$$U_{\mathrm{d,high}} = Fr_{\mathrm{v}} \sin\theta \sqrt{gD_{\mathrm{h}}(1 - \rho_{\mathrm{G}}/\rho_{\mathrm{L}})}. \tag{9}$$

The distribution coefficient, C_{O}, is estimated as

$$C_{\mathrm{O,low}} = \max\big(1.05, C_{\mathrm{O,f}}\big) + 0.15 \sin^2\theta, \tag{10}$$

$$C_{\mathrm{O,high}} = \max\big(1.2, C_{\mathrm{O,f}}\big), \tag{11}$$

where $C_{\mathrm{O,f}}$ is based on the Reynolds number as developed by Nuland (1998)

$$
\begin{aligned}
C_{\mathrm{O,f}} = C_{\mathrm{O,lam}} = 2, & \qquad Re \leq 1700; \\
C_{\mathrm{O,f}} = C_{\mathrm{O,turb}} = \frac{(n+1)(2n+1)}{2n^2}, & \qquad Re \geq 3000; \\
C_{\mathrm{O,f}} = w C_{\mathrm{O,turb}} + (1-w) C_{\mathrm{O,lam}}, & \qquad 1700 < Re < 3000;
\end{aligned}
\tag{12}
$$

with

$$w = \frac{Re_{\mathrm{slg}} - 1700}{3000 - 1700}. \tag{13}$$

The factor *n* represents the inverse exponent in the power law velocity profile for turbulent flow based on the von Karman constant ($\kappa = 0.41$),

$$n = \kappa \sqrt{2/f_{slg}}. \tag{14}$$

The wall-friction factor in the liquid slug, f_{slg}, is estimated using the modified Caetano *et al.* (1992a) approach for single-phase flows in annulus (see Appendix B).

The performance of these models and error statistical parameters with all annulus data are shown in Figure 16 and Table 6, respectively. For $Fr_M < Fr_{M,C}$, the Bendiksen (1984) model slightly under-predicts the annulus experimental data, while the Smith *et al.* (2015) approach shows a very good agreement. While it is true that both models were developed for full pipe systems, the approach of Smith *et al.* (2015) calculates the distribution parameter from the power law velocity profile, which in turn is a function of the wall-shear friction factor. The latter can be estimated for specific annulus geometries (see Appendix B) resulting in a more accurate C_O value. However, for $Fr_M \geq Fr_{M,C}$, a slight under-prediction is observed.

Based on the performance of the aforementioned models and the experimental data, a new approach is proposed for the Taylor bubble velocity in annulus flows. This approach takes, for $Fr_M < Fr_{M,C} \approx 3.3$, $U_B = U_{B,low}$ from the Smith *et al.* (2015) model. For $Fr_M \geq Fr_{M,C}$, the distribution parameter and the drift velocity are deduced from the analysis of the experimental data (see Figure 7b and Figure 8b) excluding the gas-water concentric annulus flow, as limited information was obtained at high Froude numbers. The distribution parameter, for concentric and fully eccentric annulus flows can be estimated as function of the degree of eccentricity,

$$C_O = 1.38 \left(1 - \frac{|E|}{18} \right). \tag{15}$$

Similarly, a new expression for the dimensionless drift velocity is presented,

$$Fr_d = 0.25(|E|). \tag{16}$$

Finally, the drift velocity is calculated from Eq. (2) using the hydraulic diameter, and the gas bubble velocity from Eq. (1). Our proposed approach presents an excellent agreement with data for all Froude numbers studied with a coefficient of determination very close to unity.
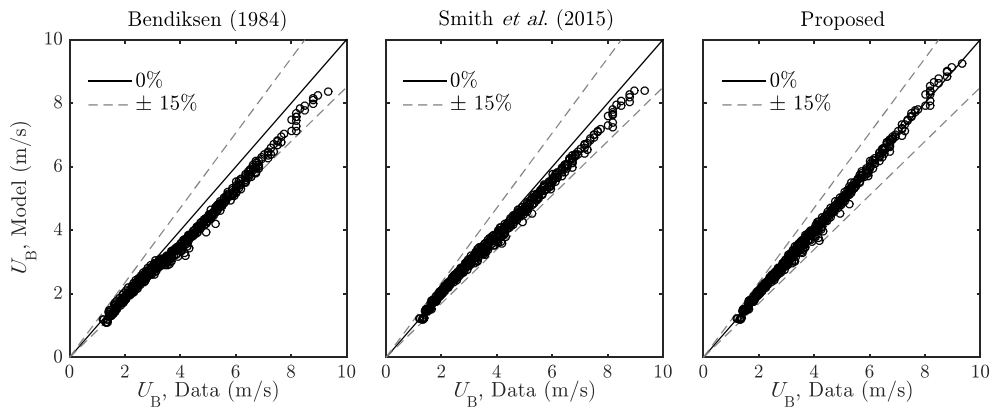
Figure 16: Slug bubble velocity models performance with all annulus experimental data.

Table 6: Error statistical parameters of the slug bubble velocity models for the concentric and fully eccentric annulus data.

		e_1 (%)	e_2 (%)	e_3 (%)	e_4 (m/s)	e_5 (m/s)	e_6 (m/s)	R^2
$Fr_M < Fr_{M,C}$	Bendiksen (1984)	−6.39	6.79	4.37	−0.147	0.154	0.102	0.882
	Smith *et al.* (2015)	0.53	2.62	3.42	0.010	0.057	0.074	0.980
All data	Bendiksen (1984)	−9.65	9.80	4.28	−0.415	0.417	0.258	0.925
	Smith *et al.* (2015)	−3.30	4.57	4.37	−0.187	0.215	0.223	0.973
	Proposed	**0.10**	**2.18**	**2.93**	**−0.0001**	**0.079**	**0.105**	**0.997**

4   Conclusions

In this work, the velocity of Taylor bubbles in concentric and fully eccentric horizontal and low-inclination upward annulus flows has been studied. The experimental data consist of average cross-sectional holdup measurements from gamma densitometers installed along the test section. The cross-correlation between two holdup profiles (as function of time) was used to calculate the gas bubble velocity for a total of 478 slug flow conditions for gas-oil and gas-water flows.

Bubbles velocities, for each flow configuration, follow a linear trend as function of the mixture velocity and can be modelled using the Nicklin *et al.* (1962) expression (Eq. (1)). For this, different experimental values of the distribution parameter, C_O, and the drift velocity, U_d, were obtained with a change in the linear trend at a critical Froude number ($Fr_{M,C} \approx 3.3$). It was found that the distribution parameter is not significantly affected by the annulus eccentricity with the exception of gas-water flows in concentric annulus for $Fr_M \geq Fr_{M,C}$. Instantaneous images from high-speed cameras revealed that the tip of the bubble nose in concentric gas-water flow is

located near the centre-line of the pipe in comparison to all other flow configurations in which the tip of the bubble nose is located in the upper region of the pipe, resulting in lower C_O values. Referring to the dimensionless bubble drift velocity, it seems that Fr_d increases with the annulus eccentricity, for $Fr_M \geq Fr_{M,C}$, and can be modelled as $Fr_d = 0.25(|E|)$, neglecting the gas-water concentric annulus data.

Inspection of the slug bubble to mixture velocity ratio revealed a transitional region at $3 < Fr_M < 6$. In general, this ratio decreases with the Froude number for $Fr_M < Fr_{M,C}$, for which $U_d > 0$, and for $Fr_M \geq Fr_{M,C}$, U_B/U_M is fairly constant, for which $U_d \to 0$ and $C_O \approx U_B/U_M$. In the transitional region, U_B/U_M increases with the Froude number resulting in negative drift velocities (from the Nicklin et al., 1962; expression). This is more prominent in gas-water flows, especially in concentric annulus, and can be related to the pipe wettability. The oil wets the pipe creating a continuous thin film around the pipe wall in the gas region for high gas velocities, whereas for water flows, this film is not continuous. This results in an irregular liquid slug front for gas-water flows, which seems to increase instabilities. This effect is enhanced in concentric annuli where the gas-pipe perimeter is larger than in fully eccentric annuli.

Analysis of individual slug bubble velocity as function of the slug length suggests two trends: (1) constant U_B for the entire range of L_S and (2) decreasing U_B with increasing L_S until a critical value. This means that slugs with $L_S < L_{CRIT}$ can have two different velocities and those with U_B higher than the mean will eventually merge with the slug ahead. However, the velocity of these slugs could not be obtained, as slugs merged before the location of the downstream gamma sensor.

The experimental data have been compared with predictions from two different models, namely, Bendiksen (1984) and Smith et al. (2015), using the hydraulic diameter of the annulus configuration. Smith et al. (2015) model shows very good agreement with data for $Fr_M < Fr_{M,C}$ and under-prediction for $Fr_M \geq Fr_{M,C}$. Therefore, a new model has been proposed based on the experimental data and the Froude number range: (1) for $Fr_M < Fr_{M,C}$, $U_B = U_{B,low}$ from the Smith et al. (2015) model, and (2) for $Fr_M \geq Fr_{M,C}$, the distribution parameter, C_O, and the

dimensionless drift velocity, Fr_d, can be estimated from Eq. (15) and Eq. (16) as function of the degree of eccentricity. This proposed model shows excellent agreement with all data, for which the absolute average relative error is 2.18%. This work presents new data for two-phase flows in horizontal and low-inclination upward annuli. Further studies are encouraged for steeper pipe inclinations, viscous oils, and different annulus diameter ratios and eccentricities in order to improve our fundamental understanding of multiphase flows in these types of geometries.

Acknowledgements

Appendix A. Error statistical parameters

The error statistical parameters for the bubble velocity as shown in Table 4 and Table 6 are given in this section. The percentage average relative error, e_1, between the experimental data, $U_{B,data}$, and predictions, $U_{B,pred}$, for a total number of samples, N, is

$$e_1(\%) = \left(\frac{1}{N} \sum_{i}^{N} \frac{U_{B,pred,i} - U_{B,data,i}}{U_{B,data,i}} \right) \times 100. \tag{A.1}$$

The percentage absolute average relative error, e_2, is

$$e_2(\%) = \left(\frac{1}{N} \sum_{i}^{N} \frac{|U_{B,pred,i} - U_{B,data,i}|}{U_{B,data,i}} \right) \times 100. \tag{A.2}$$

The standard deviation of the relative error, e_3, is

$$e_3(\%) = \sqrt{\frac{1}{N-1} \sum_{i}^{N} \left(\frac{U_{B,pred,i} - U_{B,data,i}}{U_{B,data,i}} - \frac{e_1}{100} \right)^2} \times 100. \tag{A.3}$$

The average error, e_4, is

$$e_4 = \frac{1}{N} \sum_i^N \left(U_{\mathrm{B,pred},i} - U_{\mathrm{B,data},i} \right). \tag{A.4}$$

The absolute average error, e_5, is

$$e_5 = \frac{1}{N} \sum_i^N \left| U_{\mathrm{B,pred},i} - U_{\mathrm{B,data},i} \right|. \tag{A.5}$$

The standard deviation of the error, e_6, is

$$e_6 = \sqrt{\frac{1}{N-1} \sum_i^N \left(U_{\mathrm{B,pred},i} - U_{\mathrm{B,data},i} - e_4 \right)^2}. \tag{A.6}$$

The coefficient of determination, R^2, is

$$R^2 = 1 - \frac{\sum_i^N \left(U_{\mathrm{B,data},i} - U_{\mathrm{B,pred},i} \right)^2}{\sum_i^N \left(U_{\mathrm{B,data},i} - \langle U_{\mathrm{B,data}} \rangle \right)^2}, \tag{A.7}$$

where the mean data bubble velocity is $\langle U_{\mathrm{B,data}} \rangle = U_{\mathrm{B,data}}/N$.

Appendix B. Single-phase friction factor in annulus

The friction factor in single-phase flows for non-circular pipe configurations can be estimated using the hydraulic diameter approach. However, for annulus configurations, the eccentricity of the inner pipe significantly affects the friction factor. Caetano *et al.* (1992a) proposed a geometry parameter, G, that modifies the friction factor,

$$f_{\mathrm{CON/ECC}} = f_{\mathrm{FP}} \left(G_{\mathrm{CON/ECC}} \right)^c, \tag{B.1}$$

where the full pipe Fanning friction factor for laminar flows is estimated as $f_{\mathrm{FP}} = 16/Re$ and for turbulent flows the Zigrang and Sylvester (1982) correlation can be used,

$$\frac{1}{\sqrt{f_{\mathrm{FP}}}} = -4 \log \left\{ \frac{\epsilon}{3.7 D_{\mathrm{h}}} - \frac{5.02}{Re} \log \left[\frac{\epsilon}{3.7 D_{\mathrm{h}}} - \frac{5.02}{Re} \log \left(\frac{\epsilon}{3.7 D_{\mathrm{h}}} + \frac{13}{Re} \right) \right] \right\} \tag{B.2}$$

where ϵ is the roughness of the pipe.

For the friction factor calculation in the liquid slug, the Reynolds number is defined as $Re = \rho_M U_M D_h / \mu_L$, where the mixture density, $\rho_M = \rho_L H_{LS} + \rho_G (1 - H_{LS})$, is estimated using the Gregory $et\ al.$ (1978) correlation for the slug liquid holdup,

$$H_{LS} = \frac{1}{1 + \left(\dfrac{U_M}{8.66}\right)^{1.39}}.$$
(B.3)

For concentric annulus, the geometry parameter is

$$G_{CON} = K_0 \frac{(1 - K)^2}{\dfrac{1 - K^4}{1 - K^2} - \dfrac{1 - K^2}{\ln(1/K)}},$$
(B.4)

where the empirical correction factor K_0 has been introduced to obtain a better performance for a wider range of K values and is given by

$$K_1 = 1 - |0.56 - K|,$$
(B.5)

$$K_0 = \max(0.68, K_1).$$
(B.6)

For eccentric annulus, the geometry parameter is

$$G_{ECC} = \frac{(1 - K)^2 (1 - K^2)}{4\Phi \sinh^4 \eta_0},$$
(B.7)

where

$$\cosh \eta_0 = \frac{K(1 - E^2) + (1 + E^2)}{2E},$$
(B.8)

$$\cosh \eta_1 = \frac{K(1 + E^2) + (1 - E^2)}{2KE},$$
(B.9)

$$\Phi = (\coth \eta_1 - \coth \eta_0)^2 \left[\frac{1}{\eta_0 - \eta_1} - 2 \sum_{j=1}^{\infty} \frac{2j}{e^{2j\eta_1} - e^{2j\eta_0}}\right] + \frac{1}{4}\left(\frac{1}{\sinh^4 \eta_0} - \frac{1}{\sinh^4 \eta_1}\right).$$
(B.10)

Finally, the exponent c for laminar flows is equal to unity and for turbulent flows

$$c = 0.45 e^{-(Re - 3000)/10^6}.$$
(B.11)

Note that there is a discontinuity in the exponent c at the transition between laminar ($c = 1$) and turbulent flows ($c \approx 0.45$) which can be removed by introducing an interpolation function in the transitional region. Figure B1 and Figure B2 show a comparison of single-phase friction factor data with the modified Caetano $et\ al.$ (1992a) model for different pipe diameter ratios in

the turbulent flow region ($6 \times 10^3 < Re < 10^6$). The full pipe prediction line, using the same hydraulic diameter of the annulus with $G = 1$, is also shown. Annulus friction factor values are lower and higher than the full pipe configuration for the eccentric and concentric annuli, respectively.
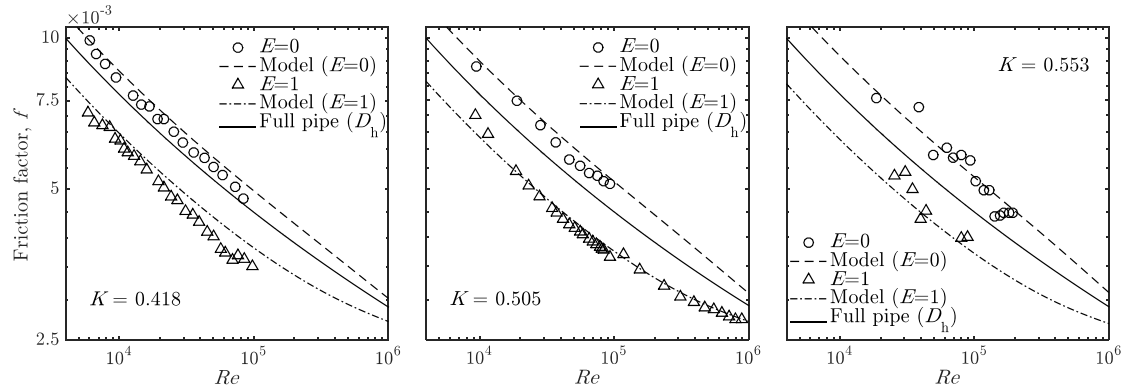
Figure B1: Comparison of the Fanning single-phase friction factor model in concentric ($E = 0$) and fully eccentric ($E = 1$) annuli with data from: (left) Tiedt (1966), (centre) current study, and (right) Caetano *et al.* (1992a).

The difference in the friction factor between the full pipe and concentric annulus reaches a maximum at $K \sim 0.55$ and a minimum as K approaches 0 or 1. A different behaviour is observed for the fully eccentric configuration where the annulus friction factor increases as K decreases but always stays lower than in a full pipe configuration. The velocity distribution in an annulus is dependent on the pipe diameter ratio and the degree of eccentricity. This has a direct effect on the wall-shear.

Referring to the model performance, good agreement is observed for the concentric and fully eccentric annuli for all pipe diameter ratios and degrees of eccentricity. This model aims to improve the prediction of the pressure gradient in annulus pipes for single-phase flows and can be used for homogenous mixtures (*e.g.* in the liquid slug).
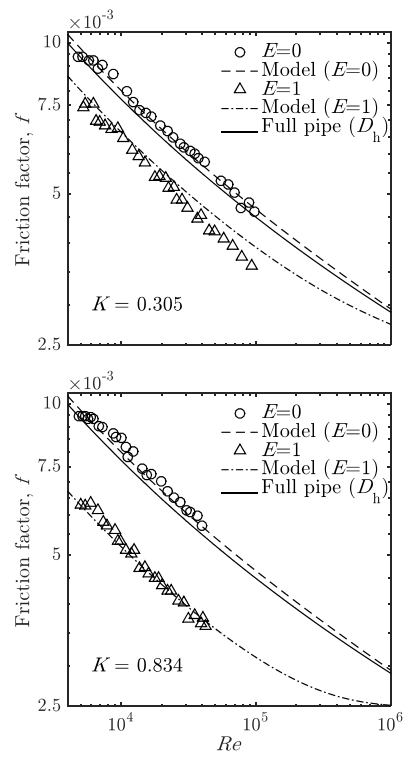
Figure B2: Comparison of the Fanning single-phase friction factor model in concentric ($E = 0$) and fully eccentric ($E = 1$) annuli with data from Tiedt (1966).

References

Alves, I.N., Shoham, O., Taitel, Y. (1993) Drift velocity of elongated bubbles in inclined pipes. Chem. Eng. Sci., 48, 3063-3070.

Bendiksen, K.H. (1984) An experimental investigation of the motion of long bubbles in inclined tubes. Int. J. Multiph. Flow, 10(4), 467-483.

Bendiksen, K.H., Langsholt, M., Liu, L. (2018) An experimental investigation of the motion of long bubbles in high viscosity slug flow in horizontal pipes. Int. J. Multiph. Flow, https://doi.org/10.1016/j.ijmultiphaseflow.2018.03.010.

Benjamin, T.B. (1968) Gravity currents and related phenomen. J. Fluid Mech., 21, 209-248.

Caetano, E.F., Shoham, O., Brill, J.P. (1992a) Upward vertical two-phase flow through an annulus-Part I: Single-phase friction factor, Taylor buble rise velocity, and flow pattern prediction. J. Energy Resour. Technol., 114(1), 1-13.

Caetano, E.F., Shoham, O., Brill, J.P. (1992b) Upward vertical two-phase flow through an annulus-Part II: Modeling bubble, slug, and annular flow. J. Energy Resour. Technol., 114(1), 1-17.

Collins, R., De Moraes, F.F., Davidson, J.F., Harrison, D. (1978) The motion of large gas bubbles rising through liquids in tubes. Int. J. Multiph. Flow, 89(3), 497–514

Crittendon, B.C. (1959) The mechanics of design and interpretation of hydraulic fracture treatments. J. Pet. Tech., 11, 21-29.

Davies, R.M., Taylor, G. (1949) The mechanics of large bubbles rising through extended liquids and through liquids in tubes. Proc. R. Soc. 200A., 375-390.

Diaz, M.J.C., Nydal, O.J. 2016. Bubble translational velocity in horizontal slug flow with medium liquid viscosity. Ph.D. Thesis, NTNU.

Dieck, R.H., 2006. Measurement Uncertainty: Methods and Aplications, Fourth ed. ISA.

Dumitrescu, D.T. (1943) Strömung an einer Luftblase im senkrechten Rohr. Z. Angew. Math. Mech., 23, 139-149.

Fagundes Netto, J.R., Fabre, J., Peresson, L. (2001) Bubble-bubble interaction in horizontal two-phase slug flow. J. Braz. Soc. Mech. Sci., 23(4), 463-470.

Gregory, G.A., Nicholson, M.K., Aziz, K. (1978) Correlation of the liquid volume fraction in the slug for horizontal gas-liquid slug flow. Int. J. Multiph. Flow, 4, 33-39.

Griffith, P. (1964) The prediction of low-quality boiling voids. J. Heat Transfer, 86, 327-333.

Hale, C.P. 2000. Slug formation, growth and decay in gas-liquid flows. Ph.D. Thesis, Imperial College London.

Hasan, A.R., Kabir, C.S. (1992) Two-phase flow in vertical and inclined annuli. Int. J. Multiph. Flow, 18(2), 279-293.

Knudsen, J.G., Katz, D.L., 1958. Fluid dynamics and heat transfer. McGraw-Hill.

Lam, H.S., 1945. Hydrodynamics. Dover Publications.

Lizarraga-Garcia, E., Buongiorno, J., Al-Safran, E., Lakehal, D. (2017) A broadly-applicable unified closure relation for Taylor bubble rise velocity in pipes with stagnant liquid. Int. J. Multiph. Flow, 89, 345-358.

Moissis, R., Griffith, P. (1962) Entrance effects in a two-phase slug flow. J. Heat Transfer, 84(1), 29-38.

Nicklin, D.J., Wilkes, J.O., Davidson, J.F. (1962) Two-phase flow in vertical tubes. Trans. Inst. Chem. Eng., 40, 61-68.

Nossen, J., Liu, L., Skjæraasen, O., Tutkun, M., Amundsen, J.E., Sleipnæs, H.-G., Popovici, N., Hald, K., Langsholt, M., Ibarra, R. (2017) An experimental study of two-phase flow in horizontal and inclined annuli. 18th International Conference on Multiphase Production Technology, Cannes, France.

Nuland, S. (1998) Bubble front velocity in horizontal slug flow with viscous Newtonian, shear thinning and Bingham fluids. 3rd International Conference on Multiphase Flow, June 8-12. Lyon, France.

Omurlu, C.M., Ozbayoglu, M.E. (2007) Analysis of two-phase fluid flow through fully eccentric horizontal annuli. 13th International Conference on Multiphase Production Technology, Edinburgh, UK.

Polonsky, L., Shemer, D., Barnea, D. (1999) The relation between the Taylor bubble motion and the velocity field ahead of it. Int. J. Multiph. Flow, 25, 957-975.

Sadatomi, M., Sato, Y., Saruwatari, S. (1982) Two-phase flow in vertical noncircular channels. Int. J. Multiph. Flow, 8(6), 641-655.

Smith, I.E., Nossen, J., Kjølaas, J., Lund, B. (2015) Development of a steady-state point model for prediction of gas/oil and water/oil pipe flow. J. Disper. Sci. Technol., 36(10), 1394-1406.

Tiedt, W. (1966) Berechnung des laminaren und turbulenten Reibungswiderstandes konaentrisher und exzentrischer Ringspalte. Chemiker-Ztg./Chem. Apparatur, 90, 813-821.

Ujang, P.M. 2003. Studies of slug initiation and development in two-phase gas-liquid pipeline flow. Ph.D. Thesis, Imperial College London.

Woods, B.D., Fan, Z., Hanratty, T.J. (2006) Frequency and development of slugs in a horizontal pipe at large liquid flows. Int. J. Multiph. Flow, 32, 902-925.

Zigrang, D.J., Sylvester, N.D. (1982) Explicit approximations to the solution of Colebrook's friction factor equation. AIChE, 28(3), 514-515.